JAAS

ROYAL SOCIETY OF CHEMISTRY

PAPER

View Article Online
View Journal | View Issue

Cite this: *J. Anal. At. Spectrom.*, 2026, **41**, 1663

A comparative study of nanosecond laser wavelengths for improved LIBS analysis of soft tissues

Hana Kopřivová,[a] Vojtěch Fedra,[a] Jakub Buday,*[ab] Daniel Holub,[cd] Petr Šperka,[b] Lucie Vrlíková,[ae] Marcela Buchtová,[e] Pavel Pořízka[ab] and Jozef Kaiser[ab]

Received 1st December 2025
Accepted 5th March 2026

DOI: 10.1039/d5ja00479a

rsc.li/jaas

Laser-based techniques, such as LIBS, enable rapid elemental detection and spatially resolved mapping of biological tissues; however, their performance strongly depends on the laser–matter interaction and the physical and chemical properties of the sample. Since every material responds differently to laser radiation, each matrix generates plasma with distinct characteristics, and the emissions of individual elements evolve uniquely during the plasma lifetime. Soft tissues, due to their natural complexity and heterogeneity, therefore, require careful optimization of measurement parameters. In this work, we systematically investigated the influence of nanosecond Nd:YAG laser wavelengths (266 nm, 532 nm, and 1064 nm), pulse energy, and gate delay for collection on LIBS analysis of mouse liver tissue in ambient air and under argon purging. For each wavelength, a defined range of pulse energies and gate delays were explored. LIBS performance was evaluated using irradiance calculations, signal-to-noise ratios, and the relative standard deviation of selected biogenic elements (Mg and Ca). Moreover, the ablation crater diameter and depth were analyzed to assess the effect of irradiation on tissues and to determine the spatial-resolution limits for LIBS elemental mapping. The results demonstrate that optimized parameter combinations significantly improved the signal quality and crater characteristics, highlighting the potential of LIBS for reliable elemental analysis of biological tissues.

Introduction

Soft biological tissues (*e.g.*, muscles, fat tissues, skin, connective tissues, *etc.*) are essential components of human and animal bodies, providing structural support, protection, and functional integration of organs. These tissues predominately contain water (50–99%) and collagen (0–35%).[1] They exhibit a complex architecture in which cells are embedded within an extracellular matrix (ECM). The ECM is composed of various biomolecules, including collagen, elastin, glycosaminoglycans, glycoproteins, and cell adhesion proteins, which together determine the tissues' mechanical and biochemical properties.[2,3] Unlike hard tissues such as bone, soft tissues are characterized by high elasticity and low stiffness, which give them a characteristic mechanical behaviour.[4] From a mechanical perspective, soft tissues are brittle and exhibit anisotropic behavior due to the fibrous arrangement of their components. These mechanical properties depend on various factors, including both physical and chemical ones (such as temperature, osmotic pressure, and pH). Microscopically, soft tissues are inhomogeneous due to their diverse and variable composition across tissue types.[2,5] Furthermore, structural specification depends on the thermal and optical properties, but, most importantly, morphological properties, which vary significantly between organs such as skin, brain, kidneys, liver, heart, and lungs.[1,6] Despite advances in biomedical imaging and biochemical analysis, accurately describing the composition and structure of soft biological tissues remains a significant challenge due to their complexity and variability.

As a promising approach to complement the existing imaging and biochemical methods, laser ablation-based techniques can provide additional information on the elemental composition and spatial distribution within soft tissues. Techniques such as Laser-Induced Breakdown Spectroscopy (LIBS) or Laser Ablation Inductively Coupled Plasma Mass Spectrometry (LA-ICP-MS) enable visualization of 2D tissue surfaces and provide insights into tissue heterogeneity that are difficult to obtain with conventional methods. These techniques utilize laser ablation, where a focused laser pulse interacts with the sample, inducing plasma formation and causing mechanical

[a]*Central European Institute of Technology (CEITEC), Brno University of Technology, Purkyňova 123, 612 00 Brno, Czech Republic. E-mail: Jakub.Buday@ceitec.vutbr.cz*
[b]*Faculty of Mechanical Engineering (FME), Brno University of Technology, Technická 2 896, 616 69 Brno, Czech Republic*
[c]*Luxembourg Institute of Science and Technology, 5 Avenue des Hauts-Fourneaux, L-4362, Esch-sur-Alzette, Luxembourg*
[d]*European Space Resources Innovation Centre, 5 Avenue des Hauts-Fourneaux, L-4362, Esch-sur-Alzette, Luxembourg*
[e]*Laboratory of Molecular Morphogenesis, Institute of Animal Physiology and Genetics, Czech Academy of Sciences, Veveří 97, 60200 Brno, Czech Republic*

and thermal damage to the tissue.[7] During laser ablation, several wavelength-dependent physical phenomena occur, including absorption, scattering, reflection, and refraction.[8] Nevertheless, the interaction between laser light and soft biological tissues is primarily influenced by their optical properties, which vary according to their composition and structure, and subsequently by the laser energy, wavelength, pulse duration, and other factors.[9,10] Scattering is significant in tissues due to their inhomogeneous microstructure, which affects the photon path length and energy deposition. However, it is known that the scattering coefficient increases with longer laser wavelengths. Reflection occurs mainly at tissue interfaces, while refraction changes the direction of propagation depending on the matrix structure.[11,12]

For laser-ablation based techniques, the most important physical parameter of the tissue impacting the laser–matter interaction is wavelength-dependent absorption. The primary contributors to optical absorption in soft biological tissues are various chromophores, including water, melanin, proteins, lipids, and hemoglobin.[2,13] Each of these molecules absorbs light differently depending on the wavelength. UV radiation ($\lambda =$ 180–400 nm) is mainly absorbed by nucleic acids, proteins, and melanin chromophores. Melanin is a highly important chromophore in skin, hair, and ocular tissues. In particular, the absorption peak in human skin is located at 335 nm. In the visible spectrum, hemoglobin and melanin are the most common absorbing chromophores, however, on a much smaller scale than in the UV region. For IR radiation, typical absorbent chromophores include hemoglobin, specific proteins, and, most importantly, water.[2,9,12] Radiation absorption is also associated with the depth of penetration after the material is ablated. In general, the depth of the ablation crater increases with increasing laser wavelength. Additionally, if the laser wavelength used is less well absorbed by soft tissues, the laser beam penetrates deeper into the tissue.[9,11,12]

Further parameters that influence the interaction of the tissue with the laser beam are the dynamics, or the duration of this interaction, which are determined by the type of laser and its pulse length. For nanosecond lasers, lasers with longer pulse lengths, there is a more prolonged exposure of the material under analysis, leading to significant heat conduction during laser ablation.[14] There is high absorption of the tailing laser energy by the microplasma, increasing the efficiency of converting laser energy into microplasma energy at the sample surface. This enhanced energy transfer subsequently leads to stronger and more efficient plasma radiation.[15,16] Compared to shorter laser pulses (ps and fs) with comparable irradiance values, it causes greater thermal damage to the sample (more ablated material from the sample surface) and better sensitivity.[14,17] When short-pulse lasers (ps and fs) are not available, selecting a suitable nanosecond laser wavelength for LIBS analysis becomes particularly important, as each wavelength interacts differently with biological tissues.

The analysis of biological tissues using laser ablation techniques like LIBS – plants,[18] teeth,[19] TagLIBS,[20,21] and soft tissues[22–24] – has been frequently used in recent years to reveal the elemental composition of samples. However, the efficiency of LIBS analyses depends crucially on various parameters, especially for biological soft tissues, such as the type of laser, laser wavelength, pulse energy, surrounding atmosphere, and detection time (gate delay). These parameters directly affect the interaction with biological tissues, microplasma formation, and the quality/intensity of the resulting data.[6,25] Since these soft matrices are dissimilar to almost any material commonly analyzed by LIBS (or other laser ablation techniques), it is necessary to perform extensive optimization analyses to provide a unified methodology for the elemental analysis of soft biological tissues.

The selection of optimal parameters for LIBS analysis has been the subject of several scientific publications.[26,27] Examples include the analysis of coal,[28] plastics,[29] soil,[30] art,[31] sediments,[32] underwater environments,[33] and different approaches to parameter optimization.[24,32] Compared to other applications, there are very few publications on the subject of selecting appropriate measurement parameters for biological tissues in general (hard tissues[34,35] and plants[36]). Although these studies clearly demonstrate the importance of parameter optimization, their conclusions are mostly application-specific and cannot be directly transferred to biological soft tissues, which exhibit very different physical and chemical properties. For soft tissues, an example is the comparison of the fundamental and fourth harmonic wavelengths of the nanosecond pulsed Nd:YAG laser (1064 nm, 266 nm) in nanoparticle-doped mouse kidneys.[37] The results of this study indicate the advantage of 1064 nm for soft tissue analysis, as it provided more reproducible laser ablation and smaller ablation craters. The reason might be that the tissue is more transparent to near-infrared radiation, allowing it to be indirectly ablated by the plasma generated on the substrate. The disadvantage of the 266 nm wavelength is that increased absorption of UV radiation by soft tissues can lead to tissue damage over a broader range. While this work included an analysis of ablation crater morphology, it was restricted to two laser wavelengths and therefore did not allow conclusions about wavelength-dependent effects. The next optimization study[38] was performed on soft tissues doped with Gd and Si nanoparticles embedded in epoxy, focusing on the laser energy (266 nm), the resulting ablation crater sizes, and spatial resolution. This study presents crater morphology for only a single laser wavelength. A challenging optimization[39] of the LIBS system for soft tissue measurements was performed using the second harmonic wavelength of the Nd:YAG laser (532 nm). Again, mouse kidneys were used for the analyses, and zinc was added as an internal standard on the surface of the soft tissue. Variables used in the optimization included defocus of the laser beam, laser energy, gate delay, gas purge, and atmosphere. Although the SNR was used as the primary optimization criterion, the physical effects of laser ablation on soft tissues, such as crater depth and morphology, were not systematically analyzed. In addition, all of the above-mentioned studies investigated biological soft tissues that were either doped with metallic nanoparticles or analyzed using an internal standard applied to the tissue surface. So, systematic optimization studies focusing on untreated soft biological tissues have not been reported in the literature. Despite the growing body of

research on LIBS applied to soft biological tissues, no study to date has systematically compared multiple nanosecond laser wavelengths together with other key experimental parameters under identical conditions within a single, unified investigation. Furthermore, the analysis of ablation crater morphology is still rarely included in optimization studies, especially for soft biological tissues. This gap highlights the need for a comprehensive optimization approach. Such an approach should combine a direct, side-by-side comparison of commonly used nanosecond Nd:YAG laser wavelengths with both spectroscopic performance evaluation and study of ablation crater characteristics.

To address these gaps, the present study proposes a comprehensive optimization strategy for LIBS analysis of soft biological tissues that combines spectroscopic performance evaluation with an extensive analysis of ablation crater morphology. The optimization is based on Signal-to-Noise Ratio (SNR), Relative Standard Deviation (RSD), and irradiance calculation as complementary metrics, together with measurements of crater diameter and depth. Nanosecond Nd:YAG laser wavelengths at 266 nm, 532 nm, and 1064 nm are systematically compared within a single experimental framework, using identical experimental conditions and the same untreated soft biological tissue matrix. The effects of laser wavelength, pulse energy, surrounding atmosphere, and detection time are examined in relation to both spectral quality and ablation crater characteristics. Based on these results, the study provides physically grounded, practically relevant guidance for selecting optimal LIBS parameters for soft tissue analysis. By combining spectral performance evaluation and ablation behavior, this work extends current optimization approaches, which are often based on spectroscopic criteria alone, and improves the reliability and reproducibility of LIBS measurements in soft biological tissues, with relevance for future biomedical and medical diagnostic applications.

Materials and methods

Sample preparation

Mouse livers embedded in paraffin blocks were analyzed as biological soft tissue model matrices. They were selected for their greater homogeneity in terms of mouse organs and their relatively large size. All animal procedures were performed in accordance with the Guidelines for Care and Use of Laboratory Animals of the Czech Academy of Sciences and approved by the Animal Ethics Committee of the Institute of Analytical Chemistry, the Czech Academy of Sciences (No. AVCR 7461/2023 SOV II).

It should be emphasized that these are real biological samples, and therefore the variability of measurements and analytical results is naturally greater compared to synthetic matrices such as gelatin, which are often used in experimental studies due to their uniform structure. However, we intended to use the most realistic matrix possible to obtain results relevant to future biomedical applications. The choice of paraffin-embedded tissues was motivated by the anticipated diagnostic use of LIBS techniques in cancer research. Paraffin embedding represents the current gold standard in routine histopathology,[40] including hematoxylin and eosin staining. However, given that histology laboratories are already overwhelmed with a growing number of tumor samples (for example, skin cancers[41]). It is unrealistic to expect that additional sample preparations, such as cryosections (or other sample preparation techniques), could be routinely performed exclusively for LIBS analysis. The acceptance of a paraffin-based routine workflow, therefore, ensures full compatibility with current diagnostic practice and increases the translational potential of this method.

The laboratory mice were sacrificed by cervical dislocation, and their livers were subsequently removed along with other organs to be used for further analysis. After removal, tissues were fixed in 4% formaldehyde for at least 24 hours. Subsequently, the tissues were washed with distilled water (approximately 12 hours) to wash out the formaldehyde. The principle of embedding involves saturating the dehydrated tissue with heated paraffin at 56 °C to 58 °C, which consists of four steps. First, tissues were dehydrated with an ethanol series (30% ethanol for 3 hours, 50% ethanol for 3 hours, 70% ethanol for 12 hours, 80% ethanol for 1 hour, 95% ethanol for 1 hour, and 100% ethanol for 1 hour). The second step was to saturate the tissue with a paraffin-dissolving fluid (xylene I, 1 hour; xylene II, 1 hour; xylene III, 1 hour). The xylene III bath was the cleanest. The third step involved saturating the tissue with paraffin (paraffin I: 1 hour; paraffin II: 1 hour; paraffin III: 12 hours; paraffin IV: 1 hour). The final step involved embedding and orienting the tissue in paraffin (HISTOWAX) and subsequent fixation. The following day, the paraffin block with the specimen was already placed in the refrigerator. The last step was to cut the sample using a sliding microtome (HM 430, Thermo Scientific, UK).

LIBS experimental system

All measurements were performed on a FireFly LIBS system (Lightigo, Brno, Czech Republic) at CEITEC, Brno University of Technology. The system consisted of a pulsed solid-state Nd:YAG laser with a fundamental emitted wavelength of 1064 nm, or the second (532 nm) or fourth (266 nm) harmonic wavelength (exchangeable within the same measuring system). The laser wavelength of 1064 nm with parameters: 6 ns pulse duration and max. energy of 20 mJ; 532 nm with parameters: 6 ns pulse duration and max. energy of 9 mJ; 266 nm with parameters: 5 ns pulse duration and max. energy of 3.6 mJ. All laser wavelengths have a repetition rate of 50 Hz and a circular laser beam (Gaussian beam profile). The laser beam was focused onto the sample surface *via* a lens with a 30 mm focal length, and plasma radiation was collected using a wide-angle (37.5 mm focal length) and optical fibre bundle (400 μm core diameter). Five Czerny–Turner spectrometers equipped with a CMOS detector were used (S1 with a range of 190–263 nm, S2 with a range of 260–370 nm, S3 with a range of 368–461 nm, S4 with a range of 460–689 nm, and S5 with a range of 690–859 nm). Further system parameters include an adjustable gate delay (μs), a gate width of 50 μs, the possibility of gas purging

(Ar), and gas extraction. Data processing was performed using the Python programming language (version 3.12.) within the Spyder IDE (version 5.5). All steps were performed using custom scripts and basic Python libraries (Matplotlib,[42] NumPy,[43] pandas,[44] and scikit-learn in current versions[45]).

Profilometry

A 3D optical profilometer, the Contour GT-X8 (Bruker, Tucson, USA), based on white-light interferometry, was used for high-resolution surface analysis of samples (nanometer vertical resolution). The crater diameter and depth after laser ablation were measured using vertical scanning interferometry (VSI) mode at all laser pulse energies, the surrounding atmosphere (Ar purge/NO–Ar purge), and different wavelengths (266 nm, 532 nm, and 1064 nm). The diameters and depths of laser ablation craters were evaluated for at least 10 craters at each energy level, from which the average was then calculated. Proprietary evaluation software Bruker's Vision64 was used for data evaluation, processing, and visualization.

For crater diameter measurements, at least five crater-edge points were manually marked around each ablation crater, after which a circle fit was performed to determine the diameter (Fig. 1A). This manual approach was chosen due to the fact that craters in soft biological tissues are mechanically strongly disrupted and inhomogeneous, making it really difficult to reliably capture their edges with a computer-assisted approach. All measured values for a single measurement setting were averaged, and the mean value, along with its standard deviation, was calculated. Crater depth values (Fig. 1B) were obtained by defining a reference region of the sample surface without laser ablation (marked in red, R) as the zero level. Subsequently, the entire ablation crater was selected (marked in green, M). The average depth of the whole ablation crater, together with the corresponding standard deviations, was calculated. Consequently, the values reported in the results do not represent the maximum crater depths, but rather the mean depths averaged over the entire crater area. However, due to variable crater shapes, only the average depth is reported, as calculating the ablated volume would be unrealistic for soft-tissue matrices.

Experimental methodology

The parameters for each Nd:YAG laser wavelength (λ) were optimized (266 nm, 532 nm, and 1064 nm). These direct parameters, which significantly influence the signal results, include the laser pulse energy (E, mJ), gate delay (GD, μs), and the surrounding atmosphere in the ablation chamber (air/argon). The optimized indirect parameters include the diameters and depth of the ablation craters formed.

The measurements were performed to optimize the ideal parameters for mapping the samples. The experimental setup had a spatial resolution of 250 × 250 μm in both the x and y axes, without shot accumulation. First, mouse liver samples were analyzed using 20 laser-shot scans. For all three Nd:YAG laser wavelengths (266 nm, 532 nm, and 1064 nm), measurements were performed across a range of laser energies (from maximum) and gate delays (GD) with an interval of 0.1/0.2 μs. The maximum GD values were 1.2 μs at 266 nm and 532 nm and 1.4 μs at 1064 nm, due to the intensities (and, consequently, the irradiance – see Results and discussion) decreasing for all wavelengths as the GD increased. Therefore, it was not necessary to continue with higher GD values. Each wavelength was evaluated both under atmospheric conditions and with an argon purge. Specific energy steps and gate-delay intervals used for each wavelength are summarized in Table 1.

For the ideal parameters determined from the initial measurements described above for all wavelengths, mouse liver samples with a higher number of laser shots (approximately 300) were subsequently analyzed to evaluate the optimal results more accurately. This extended experiment yielded nearly identical results to the initial experiment; therefore, for brevity, we present the results only from the initial experiment in the Results and discussion section.

All results were evaluated using SNR (Signal to Noise Ratio) analysis and RSD (Relative Standard Deviation) analysis for the most important and most intensive spectral lines like calcium (Ca II 393.37 nm, Ca II 396.85 nm, and Ca I 422.67 nm), magnesium (Mg II 279.55 nm and Mg II 280.27 nm), sodium (Na I 589.00 nm and Na I 589.59 nm), and potassium (K I 766.49 nm and K I 769.90 nm). The crater diameters and depth values were measured using a profilometer (based on the principle of scanning interferometry), and it was possible to calculate irradiance values (GW cm^{-2}) for each measurement. This parameter is essential because, in general, the smaller the diameters of the craters, the more advantageous the LIBS technique is for potential soft tissue mapping, as improved spatial resolution results in more detailed sample characterization. The results were then summarized using heat maps, which plot the calculated irradiation intensity values on the x-axis and the signal acquisition GD on the y-axis. The color scale on the heat map

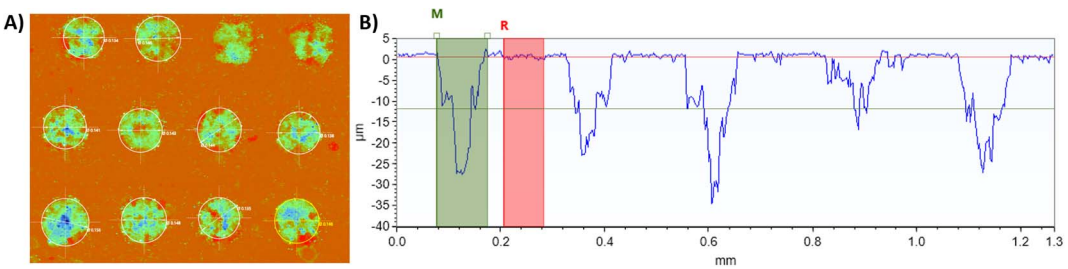

Fig. 1 (A) Manually marked edge points for crater diameter calculations; (B) methodology for crater depth analyses.

Table 1 Experimental conditions applied for LIBS measurements at 266, 532, and 1064 nm

Laser wavelength	Pulse duration (ns)	Laser energy (mJ)	Gate delay (μs)
266 nm	5 ns	3.6–2.4 (step: 0.4 mJ)	0–0.8 (step: 0.1), 1.0, and 1.2
532 nm	6 ns	9–4 (step: 1 mJ)	0–0.8 (step: 0.1), 1.0, and 1.2
1064 nm	6 ns	20–3 (step: 1 mJ)	0–0.8 (step: 0.1), 1.0, 1.2, and 1.4

represents SNR values. The white areas correspond to GD values for which no measurements have been made.

Data processing methodology

All steps of the data processing methodology were performed in the Spyder interface of the Python programming language using custom scripts. First, data were uploaded to the interface. The maximum spectrum of each measurement set was investigated to confirm the attributes of the selected spectral lines and the noise areas. This step was crucial to ensure that the noise area did not include any artifacts or very low-intensity spectral lines, and the spectral lines selected for further analysis were present in the spectrum and did not exhibit signs of self-reversal, severe self-absorption, or other degradation effects.

Before calculating the SNR, all spectra were background-subtracted using the asymmetrically reweighted penalized least squares smoothing algorithm[46] using parameters $\lambda = 105$ and $p = 0.0001$. The spectral line maximum intensity and noise standard deviation from the close vicinity of the selected line were taken from these background-corrected spectra to calculate the SNR values. Due to the gradual increase in laser power during the first several laser pulses of the measurement, the values from the first five shots of each row were omitted from the data set to increase the uniformity of the measurement conditions within a set. The SNR values were then filtered based on the normal distribution of values, where the minimum and maximum 10% of values were labeled as outliers and removed from the dataset. To calculate RSD (%), the standard deviation of the data was divided by the average and multiplied by 100 to obtain the percentage. The final SNR and RSD values shown in the Results and discussion section were calculated from the remaining data values. Irradiance (I_e, GW cm^{-2}) was calculated based on the laser energy (E, mJ), pulse length (t, ns), and crater size (S, mm^2). The laser energy was converted to radiant flux (θ_e, W) by accounting for the pulse length, and the resulting radiant flux was then divided by the irradiated surface area to obtain the irradiance.

Results and discussion

Profilometry analyses

Profilometric evaluation revealed distinct differences in the crater diameter and depth across all three Nd:YAG wavelengths (266 nm, 532 nm, and 1064 nm) and all investigated energies. All measurements were performed under atmospheric conditions and with argon purging.

Crater diameter. The average values for each energy were obtained from 10 measurements. Fig. 2 shows graphs of the diameters of ablation craters for each wavelength/energy/Ar purge/NO–Ar purge. It also contains profilometry scans of the surface of the soft tissues with laser ablation craters. In general, it can be concluded that ablation craters are, in the majority of cases, larger in the presence of argon purging. The results also show that the largest crater diameters in soft tissues were produced using a second-harmonic wavelength (532 nm) laser, and the lowest values were obtained with a 1064 nm laser, as shown by the profilometric analysis. The phenomena affecting the size of ablation craters and their wavelength dependence are described below.

The 266 nm laser exhibits almost identical crater diameters at the two lowest energies, both with and without argon purging. This trend thereafter changes. The results also show an increase in crater diameter with higher laser energy, indicating higher ablation efficiency. The maximum diameter is approximately 0.13 mm. At this UV wavelength, the laser radiation is efficiently absorbed by the biological tissue, leading to highly

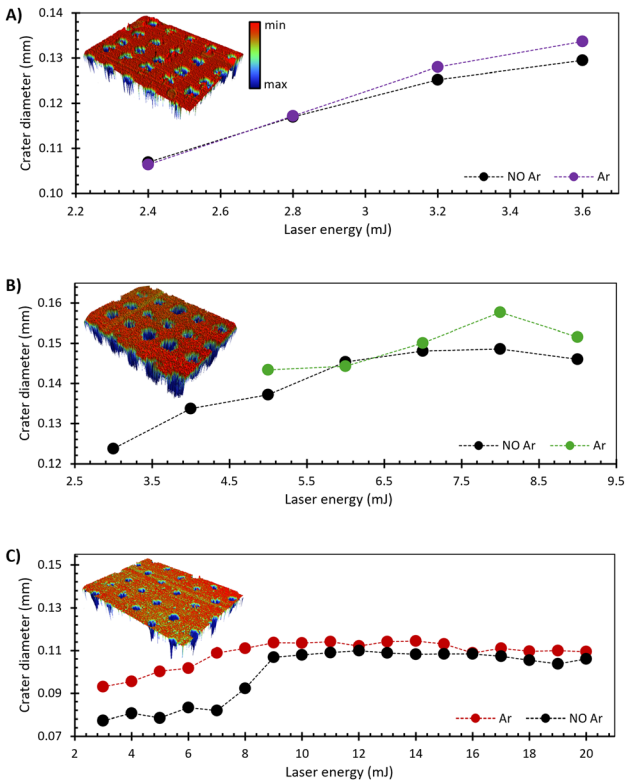

Fig. 2 Graphs showing the average diameters and profiles of laser ablation craters for laser wavelengths: (A) 266 nm, (B) 532 nm, and (C) 1064 nm, with and without argon purging.

localized energy deposition. Ablation, therefore, occurs with minimal plasma shielding due to the formation of a laser-supported combustion (LSC) wave, allowing efficient coupling of laser energy to the target and generating a compact, dense plasma plume with a relatively short lifetime.[47,48] In the presence of argon, reduced plasma shielding allows more laser energy to reach the sample, resulting in a larger amount of ablated material and potentially resulting in a slightly larger ablated area.[49] The surface scan of the matrix reveals that for this wavelength, the formation of debris around the crater is high after the laser ablation of the biological matrix. On average, the Ar-purged measurements showed a standard deviation of about 1.3, while the no-purge averaged around 1.2.

The most significant tissue damage occurred at 532 nm because of the tissue's low absorption, leading to greater thermal spreading. This is evident not only from the crater diameters, which reach approximately 0.15 mm, but also from analysis of the biological soft tissue surface. The craters are not smooth, and the surrounding tissue is severely damaged. Standard deviations for almost all diameter measurements were around 0.006–0.01 mm. The graph also shows that the crater diameters remain almost constant for both series (Ar purge/NO–Ar purge) from an energy of 6.5 mJ.

The red laser (1064 nm) produces the smallest ablation crater. An interesting trend is that above an energy of 9 mJ, the crater diameter stabilizes at around 0.11 mm and does not increase further, or even slightly decreases, up to the maximum energy of 20 mJ. This behavior reflects a stabilization of the effective energy deposited into soft tissues at higher laser energies. An increasing fraction of the laser energy interacts with the evolving plasma rather than being directly deposited into the target, leading to enhanced plasma shielding and laser-supported detonation (LSD) expansion. Consequently, further increases in laser energy primarily contribute to plasma growth and background emission rather than to increased ablation efficiency or crater enlargement.[47,48,50] The presence of an argon atmosphere slightly increases crater diameters by reducing plasma energy losses and enabling more efficient energy transfer to the sample; however, this effect remains secondary to plasma shielding at 1064 nm. Across the dataset, the diameter measurements showed standard deviations of about 0.0075–0.01 mm with an Ar purge, whereas without an Ar purge, the values were slightly higher, approximately 0.009–0.011 mm. The crater profile reveals very little mechanical tissue damage, with almost no debris formation.

For high-resolution LIBS mapping, the 266 nm laser is the most favorable from the perspective of crater diameter, as it results in efficient tissue absorption. This allows for the use of the finest spatial resolution without overlapping thermally affected zones.[2] At higher laser energies (532 nm and 1064 nm), where there is minimal laser absorption, intense energy transfer generates pronounced local thermal degradation and coagulation around the ablation crater, creating a significant heat-affected zone that extends beyond the visible crater edge. This thermal damage can modify local mechanical properties and slightly change the mechanical and chemical composition, potentially affecting both the ablation efficiency and the LIBS signal (*e.g.*, intensity, SNR, and elemental distribution).[6] Consequently, high-resolution mapping of large tissue areas may include thermally modified regions, which could lead to biased or inconsistent semi-quantitative or potentially quantitative results. To mitigate these effects, lower spatial resolution is recommended, ensuring that ablation spots do not overlap previously altered zones. Further study of heat diffusion and matrix changes under high-energy irradiation would be necessary to fully assess these limitations.

Crater depth. All average values for ablation crater depth were calculated from 7 to 10 values and then averaged. It is essential to mention that these are not maximal crater depths, but rather average depths across the entire ablation crater area. Fig. 3 shows the depths for the three wavelengths, with results for measurements with and without argon purging displayed for each wavelength. Although the differences in crater depth are less pronounced than those in crater diameter, systematic variations related to laser wavelength, pulse energy, and ambient atmosphere are still evident. For all measurements of different wavelengths, the depth of ablation craters increases relatively continuously with rising energy. The side profiles (shown in color in the lower left corner of Fig. 3) clearly demonstrate that each wavelength produces distinct crater morphologies, reflecting different ablation mechanisms and energy–tissue interaction regimes. In an overall comparison, it can be stated that the deepest craters for biological soft tissues are formed by a laser with a wavelength of 532 nm, followed by a red laser (1064 nm). The UV laser (266 nm) has the least effect

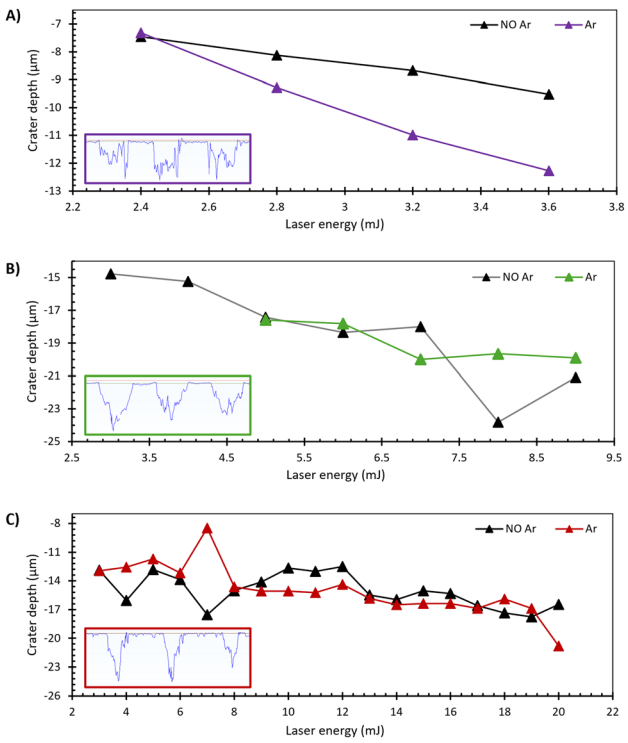

Fig. 3 Graphs showing the average depths and side profiles of laser ablation craters for laser wavelengths: (A) 266 nm, (B) 532 nm, and (C) 1064 nm, with and without argon purging.

on crater depth in soft tissues. This trend indicates that crater depth is strongly influenced by the wavelength-dependent optical absorption of biological tissues, in addition to laser pulse energy and plasma dynamics.

With a 266 nm laser, the crater depth increases linearly with rising energy. The maximum average depth (11.77 μm) can be observed at an energy of 3.6 mJ with argon purging (standard deviation: 1.4–2.6 μm). In measurements without purging, the maximum depth also occurs at an energy of 3.6 mJ, but the value is 9.02 μm, representing a decrease of almost a quarter (standard deviation: 1.2–2.5 μm). This difference can be attributed to the longer plasma lifetime under an argon atmosphere, which prolongs plasma–surface interaction and enhances energy transfer to the soft biological matrix. The side profiles reveal a strongly inhomogeneous crater shape, consistent with highly localized ablation governed by strong UV absorption and minimal thermal diffusion into the surrounding tissue.

For a wavelength of 532 nm, a downward trend is also visible, although it is not as linear. The difference in depth between measurements with and without argon is also not as significant. It can be concluded that for measurements with argon, the depth of the craters formed stabilizes at higher energies (7–9 mJ). However, this is not applicable to measurements taken under atmospheric conditions. The maximum depths reach around 20–23 μm. The crater profiles at this wavelength are generally smoother and more regular; however, extensive thermal damage to the surrounding tissue is expected. Due to the relatively low absorption of biological soft tissues at 532 nm, a significant fraction of the laser energy is converted into heat rather than being directly absorbed by the matrix. This promotes enhanced thermal diffusion into the surrounding tissue, resulting in deeper craters and a pronounced heat-affected zone extending beyond the visible crater boundary. Regarding the standard deviation, the values are nearly identical for all measurements with Ar purging, ranging from 2.1 to 2.5 μm. The standard deviation for measurements without purging is inconsistent, 1.4 to 3.6 μm.

At the fundamental wavelength (1064 nm), deeper craters are visible at lower wavelengths for analysis without argon, although this trend reverses from middle energies (8 mJ). Deeper craters are then observed again with the argon purge, as with the 4th harmonic wavelength. The red laser penetrates deep into the tissue, with maximum depths of around 18–20 μm. The 1064 nm laser penetrates moderately into the tissue, producing well-defined crater profiles with limited lateral material removal. Due to the tissue's moderate absorption at 1064 nm, a significant fraction of the laser energy interacts with the evolving plasma rather than being deposited directly into the tissue. This interaction enhances plasma shielding and promotes LSD expansion, which constrain further increases in crater depth at higher laser energies. Standard deviations for measurements with an Ar purge are, in most cases, around 2.5 μm (with three values around 4.0 μm), and for measurements without an Ar purge, they are very similar.

The comparison of crater depths for all wavelengths at the same energies is also quite interesting. For instance, at an energy of 3 mJ. For a 1064 nm laser, the depth of the resulting ablation crater is 12.9 μm, for a 532 nm laser, it is 14.7 μm, and for a 266 nm laser, it is 7.9 μm without Ar and 9.64 μm with Ar present. The values for 266 nm wavelength are recalculated (linear fit) due to the highly linear relationship between the laser pulse energy and the resulting crater depth. In general, it can therefore be concluded that, in terms of tissue damage about the depth of the ablation crater, analysis in the UV range is the least damaging for biological soft tissues.

Signal-to-noise ratio and relative standard deviation analyses. The second part of the study involved analyzing the signal-to-noise ratio (SNR), calculating the relative standard deviation (RSD), and irradiance for all measurement combinations, *i.e.*, for all three types of lasers, their energies, and gate delays. Irradiance calculations were performed because it is easier to reproduce and simulate these values on other LIBS systems than if only energy values were provided. All results are presented in the following heat maps for easier orientation among the large number of results. The results for all visible biogenic spectral lines of magnesium (Mg II 279.55 nm and Mg II 280.27 nm), calcium (Ca II 393.37 nm, Ca II 396.85 nm, and Ca I 422.67 nm), sodium (Na I 589.00 nm and Na I 589.59 nm), and potassium (K I 766.49 nm and K I 769.90 nm) were processed (Fig. 4). The results in the article are only presented for magnesium due to the large number of results, and also because magnesium is the most significant element in terms of tumor diagnosis, so it receives the most emphasis.[24] The results for the other elements are attached in the SI.

It is essential to note that all analyses were conducted on a real biological matrix (mouse liver), where measurements (*e.g.*, for a single laser wavelength/gas purging) could not be performed on a single sample due to the size of the mouse organ and the size of the paraffin blocks. The binding of biogenic elements in the biological matrix and sample preparation, as well as potential leaching (the partial loss or redistribution of elements) when using formaldehyde and subsequently alcohol series, also play a significant role. Magnesium (Mg^{2+}) is strongly bound to several enzymes, nucleic acids, and others, so this element is not washed out. It is therefore completely safe to use this element in semi-quantitative comparisons between samples.[51] Calcium (Ca^{2+}) is present in tissues in several forms. However, the primary form is strongly bound to mainly proteins/phospholipids and the extracellular matrix. Therefore, only a small amount of leaching is expected to occur during preparation.[52] Sodium (Na^{+}) and potassium (K^{+}) are mainly present in tissues in the form of free ions in the extracellular matrix. Therefore, the amount of these two elements is strongly influenced by sample preparation.[52] Consequently, it is necessary to exclude these results (for Na and K) from the experiment, since they showed extreme differences between individual livers due to the problem mentioned above. One should also take into account that although we have selected the most homogeneous biological matrix possible according to biologists, these biological tissues are still highly heterogeneous compared to inorganic materials, such as metals, and therefore fluctuations in the results may occur due to slightly different sample hardness,

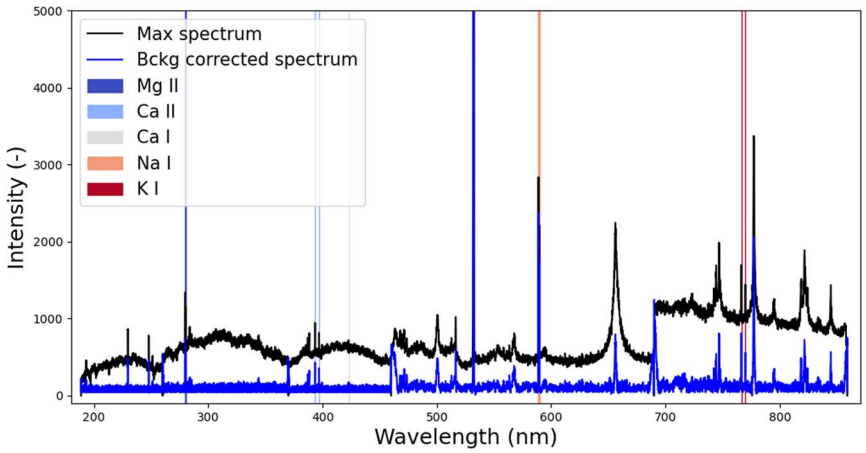

Fig. 4 Maximal and background-corrected spectrum with highlighted spectral lines of interest for 532 nm laser wavelength.

microscopic changes in the morphology of the sample surface, or even the paraffin component in the sample.

266 nm. For the UV laser, four sets of measurements were always performed, starting from a maximum energy of 3.6 mJ (0.4 mJ steps). The results for the magnesium spectral line – Mg II 279.55 nm (Fig. 5A) – show that higher SNR values are obtained for measurements with argon purging, where the SNR reaches its highest value of approximately 14. This behavior can be attributed to the presence of argon, which prolongs the plasma lifetime and reduces energy losses to the surrounding gas, resulting in a denser and more stable plasma plume. The maximum SNR values for measurements under atmospheric conditions ranged from 9.5 to 10.5. Under both conditions, the highest SNR values are observed at the shortest GDs, specifically between 0.0 μs and 0.2 μs. At these early times, the plasma is characterized by high temperature and electron density, leading to strong emission intensity.[53] A slightly longer gate delay of 0.3 μs still provides sufficiently good performance for argon purged measurements, indicating that the plasma remains radiatively active for a longer time in argon. The corresponding RSD heatmaps (Fig. 5B) reveal maximum values of approximately 20–21%. Elevated RSD values at the shortest gate delays are associated with strong fluctuations in plasma temperature and electron density during the initial stages of plasma formation.[54] There is also a visible difference in measurements without purging, which show a higher number of increased RSD values than measurements with argon. This result can be attributed to the fact that when analyzing biological soft tissues with gas purge, the measurements are more stable. When converted to irradiance from individual energies, it was found that using higher UV laser energies, specifically 3.2 mJ or 3.6 mJ, is most effective. The resulting irradiance values were similar for all energies, with a maximum irradiance of 5.87 GW cm^{-2} for Ar purge and 5.91 GW cm^{-2} for NO/Ar purge measurements.

532 nm. Different numbers of measurements can be observed for individual categories at this wavelength. This is explained by the very weak signals measured at lower energies in argon measurements (9 mJ–5 mJ/1 mJ step) compared to analysis under atmospheric conditions (9 mJ–3 mJ/1 mJ step). This observation indicates that green radiation is less efficiently

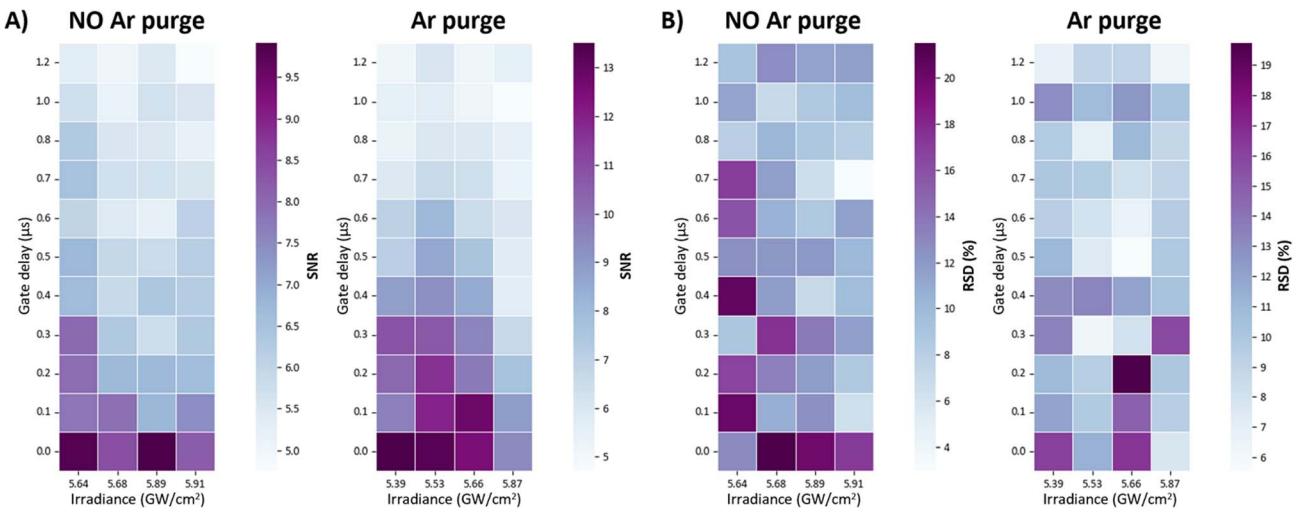

Fig. 5 Heat maps of (A) SNR and (B) RSD analyses for Mg II 279 nm without/with Ar purging for 266 nm laser wavelength.

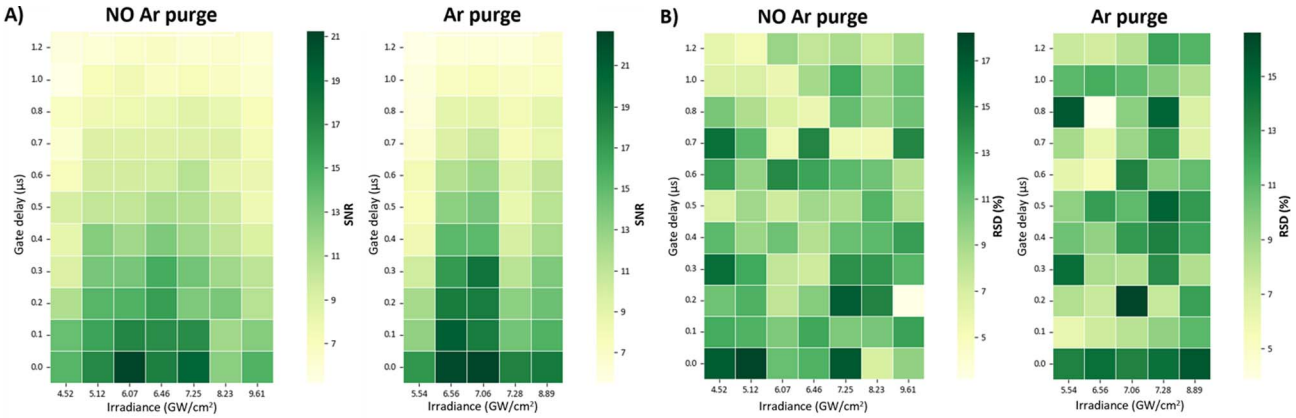

Fig. 6 Heat maps of (A) SNR and (B) RSD analyses for Mg II 279 nm without/with Ar purging for 532 nm laser wavelength.

absorbed in soft tissues than UV radiation, as the UV signal remains detectable at lower irradiance values at which the green signal is already lost. The SNR results (Fig. 6A) show a similar trend, with slightly higher SNR values visible for measurements with argon purging. The maximum values are around 22.5 for measurements with an Ar purge and 21 for measurements under atmospheric conditions. The highest SNR values are visible at middle energies for 7 mJ and 6 mJ in both sets. The highest SNR values are also visible for lower GD values. Without an argon purge, 0.0 µs or 0.1 µs are the most suitable options. For the second set, *i.e.*, with argon, high SNRs are observed, and the range of usable GDs is much larger, from 0.0 µs to 0.3 µs. This reflects argon's ability to stabilize and prolong the plasma emission. RSD analysis (Fig. 6B) indicates that higher values are present in measurements without argon (18%) than in analyses with argon purging (16%). However, the number of high RSD values is similar for both cases, suggesting that plasma stability at this wavelength is influenced more by sample heterogeneity than by atmospheric conditions. The calculated irradiance

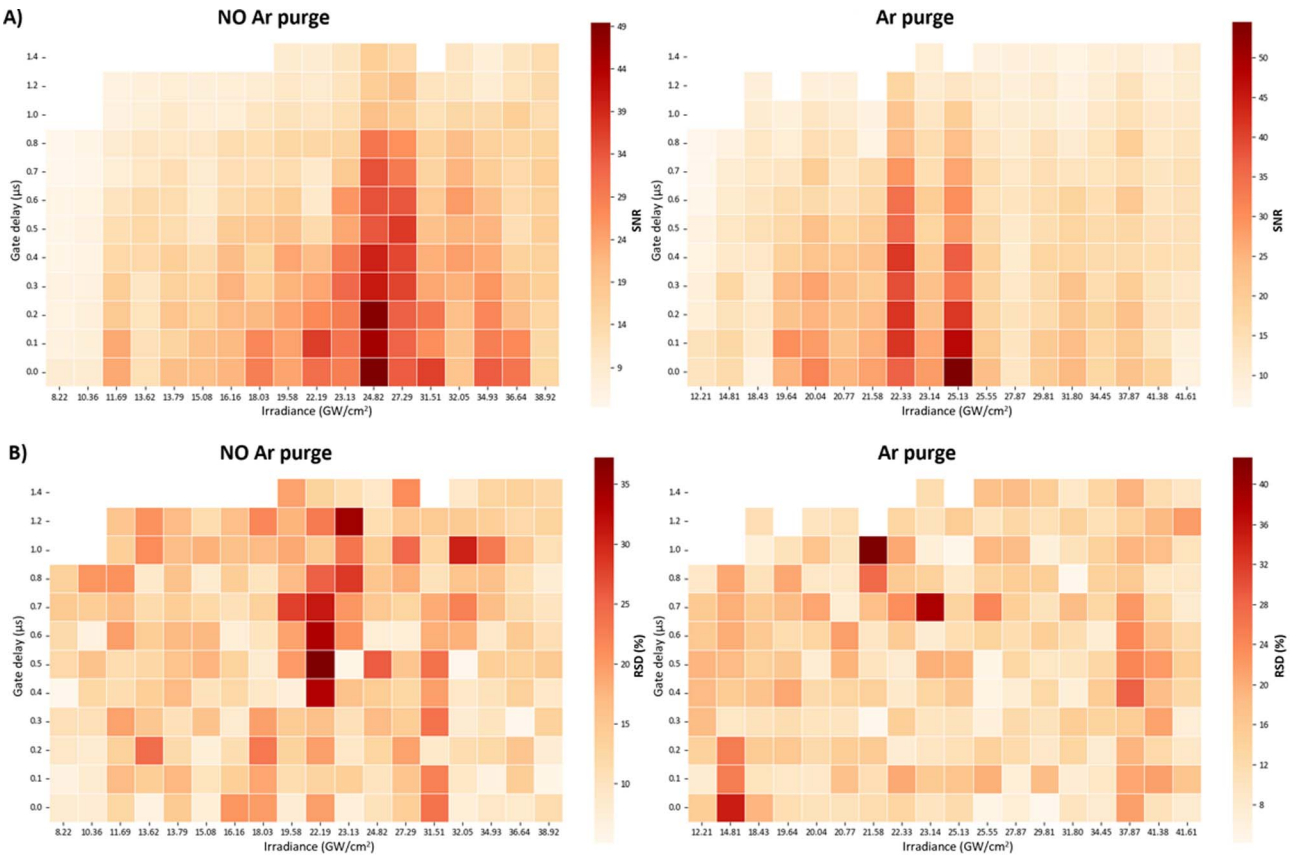

Fig. 7 Heat maps of (A) SNR and (B) RSD analysis for Mg II 279 nm without/with an Ar purge for 1064 nm laser wavelength.

values reach 9.61 GW cm^{-2} for measurements without argon and 8.89 GW cm^{-2} with argon purging.

1064 nm. Eighteen sets of measurements were performed under both conditions (Ar purge/NO–Ar purge) for the fundamental wavelength (1064 nm). Again, a trend is evident in Fig. 7A, where the maximum SNR values are lower under atmospheric conditions (approximately 49) than with argon purging (approximately 53). At this wavelength, the largest difference between the two sets of analyses is apparent. At this wavelength, the influence of argon is most pronounced, reflecting strong plasma–gas interactions in the infrared regime. The highest SNR values are observed at medium pulse energies of 10–12 mJ. At higher energies, increased plasma shielding limits further energy coupling into the sample, despite higher incident irradiance. This effect is associated with inverse Bremsstrahlung absorption, which scales with the square of the laser wavelength and leads to the formation of large, spatially extended plasma plumes.[48] An increase in the usability of higher GDs for obtaining optimal results can also be noticed. GDs with durations of up to 0.6 μs can be used for measurements with and without argon. However, it should be emphasized that the highest values are again for GDs of 0.0–0.2 μs. This time, the results for RSD (Fig. 7B) are higher for measurements with argon purging (42%) than for measurements without gas (36%), but only for two measurements. Nevertheless, the number of high values is again higher for measurements without purging, indicating greater measurement instability. The higher overall variability at 1064 nm can again be attributed to plasma shielding and plume morphology instability, which increase the shot-to-shot fluctuations. This instability could be suppressed by adding some internal standardization. The final irradiance calculations yield very high values, specifically 38.92 GW cm^{-2} for the Ar purge and 41.61 GW cm^{-2} for the NO/Ar purge. Although high irradiance values improve the SNR, they also cause pronounced thermal and mechanical damage to soft biological tissues, which must be considered when selecting optimal parameters.

When comparing the same pulse energy (3.6 mJ/4 mJ) across all wavelengths, the highest irradiance is achieved at 1064 nm, followed by 266 nm and 532 nm. In terms of SNR, the highest values are obtained for 1064 nm, followed by 532 nm and 266 nm. In general, soft tissue ablation produces plasmas with short lifetimes, making short gate delays the most suitable choice across all wavelengths. Argon purging improves the measurement stability and reproducibility by extending the plasma lifetime and stabilizing plasma evolution, particularly for UV excitation. When comparing RSD values for argon purged measurements, 266 nm and 1064 nm show the most favorable performance, except for a few outliers. The results for calcium spectral lines follow a similar trend, with shorter GDs yielding the best results. Other parameters vary slightly. A more detailed comparison can be found in the SI.

Conclusion

This study presents an optimized experimental framework for LIBS analysis of biological soft tissues, a matrix type for which comprehensive optimization studies have so far been largely absent in the literature. By evaluating three Nd:YAG laser wavelengths (266 nm, 532 nm, and 1064 nm) in combination with laser energy, data acquisition timing, and atmosphere – Ar purge *versus* NO/Ar purge, this work demonstrates how laser–tissue interaction and plasma dynamics directly affect both analytical performance and tissue damage.

Profilometric analysis revealed pronounced wavelength-dependent differences in crater diameter and depth, reflecting distinct ablation mechanisms in soft biological tissues. UV irradiation at 266 nm produces shallow and laterally confined craters with minimal thermal diffusion, making it the least invasive option and particularly suitable for high-resolution elemental mapping. In contrast, excitation at 1064 nm yields smaller crater diameters but greater penetration depths, enabling improved signal intensity at the cost of increased thermal load. The 532 nm wavelength consistently results in extensive thermal damage, irregular crater morphology, and large heat-affected zones, which limit its applicability for routine LIBS analysis of soft tissues. These morphological differences are directly reflected in plasma behavior and analytical performance. For all wavelengths and biogenic elements studied, optimal LIBS performance is achieved at short gate delays. While the highest SNR values are achieved at 1064 nm, followed by 532 nm and 266 nm, increased radiation intensity, especially in the IR region, increases plasma shielding and fluctuations between individual shots, limiting further increases in analytical reliability. This effect is also reflected in the RSD behavior: for infrared excitation, the highest variability is observed at longer gate delays, whereas for UV excitation, higher RSD values occur primarily at very short delays immediately after ablation. Argon purging generally improves signal stability and reproducibility by prolonging the plasma lifetime and reducing energy losses, with the greatest benefits observed with UV excitation. When crater morphology, plasma evolution, and analytical metrics are considered together, careful adjustment of wavelength, irradiance, gate delay, and ambient atmosphere proves essential for balancing signal quality, spatial resolution, and tissue integrity.

By linking ablation characteristics to plasma dynamics and LIBS performance, this study provides practical guidance for selecting experimental parameters suited to complex biological tissues. These findings support the use of LIBS as a promising tool for spatially resolved elemental analysis in biomedical research and contribute to its further development towards medical diagnostic applications.

Author contributions

Hana Kopřivová: conceptualization, LIBS analysis, data processing, data interpretation, visualization, writing; Vojtěch Fedra: LIBS analysis, profilometric analysis, data processing; Jakub Buday: LIBS analysis, writing; Daniel Holub: data processing, writing; Petr Šperka: profilometric analysis, funding; Lucie Vrlíková: sample preparation; Marcela Buchtová: supervision; Pavel Pořízka: supervision; Jozef Kaiser: supervision, funding.

Conflicts of interest

There are no conflicts to declare.

Data availability

Data are available at: https://doi.org/10.5281/zenodo.18376509.

Supplementary information (SI) is available. See DOI: https://doi.org/10.1039/d5ja00479a.

Acknowledgements

HK (Brno PhD Talent Scholarship Holder – funded by the Brno City Municipality) acknowledges the support provided by the specific grant from CEITEC, Brno University of Technology (CEITEC VUT-J-24-8599 and CEITEC VUT-J-25-8897). PP gratefully acknowledges the support from TAČR NCK CAEPO (project no. TN02000020; subproject TN02000020/003N) and the Czech Science Foundation (no. 25-16166S).

References

1 A. Vogel and V. Venugopalan, Pulsed Laser Ablation of Soft Biological Tissues, in *Optical-Thermal Response of Laser-Irradiated Tissue*, Springer Netherlands, Dordrecht, 2010, pp. 551–615, DOI: 10.1007/978-90-481-8831-4_14.

2 A. Vogel and V. Venugopalan, Mechanisms of Pulsed Laser Ablation of Biological Tissues, *Chem. Rev.*, 2003, **103**(2), 577–644, DOI: 10.1021/cr010379n.

3 H. Jelínková, Introduction: the history of lasers in medicine, in *Lasers for Medical Applications*, Elsevier, 2013, pp. 1–13. doi: DOI: 10.1533/9780857097545.1.

4 G. A. Holzapfel, Biomechanics of Soft Tissue, in *Handbook of Materials Behavior Models*, Elsevier, 2001, pp. 1057–1071, DOI: 10.1016/B978-012443341-0/50107-1.

5 J. D. Humphrey, Review Paper: Continuum biomechanics of soft biological tissues, *Proc. R. Soc. London, Ser. A*, 2003, **459**(2029), 3–46, DOI: 10.1098/rspa.2002.1060.

6 M. H. Niemz, *Laser-Tissue Interactions*, Springer International Publishing, Cham, 2019, DOI: 10.1007/978-3-030-11917-1.

7 K. A. Brackett, Tissue Interactions of Nd:YAG Lasers, in *Advances in Nd: YAG Laser Surgery*, Springer New York, New York, NY, 1988, pp. 336–343, DOI: 10.1007/978-1-4612-3728-0_43.

8 L. Carroll and T. R. Humphreys, LASER-tissue interactions, *Clin. Dermatol.*, 2006, **24**(1), 2–7, DOI: 10.1016/j.clindermatol.2005.10.019.

9 G. Insero, *et al.*, The safe use of lasers in biomedicine: Principles of laser-matter interaction, *J. Public Health. Res.*, 2023, **12**(3), DOI: 10.1177/22799036231187077.

10 M. M. Jawad, *et al.*, An Overview of Laser Principle, Laser-Tissue Interaction Mechanisms and Laser Safety Precautions for Medical Laser Users, *Int. J. Pharmacol.*, 2011, **7**(2), 149–160, DOI: 10.3923/ijp.2011.149.160.

11 M. H. Niemz, *Laser-Tissue Interactions*, Springer Berlin, Heidelberg, Berlin, Heidelberg, 1st edn, 1996, DOI: 10.1007/978-3-662-03193-3.

12 J. T. Walsh *et al.*, Pulsed Laser Tissue Interaction, *Optical-Thermal Response of Laser-Irradiated Tissue*, Dordrecht, Springer Netherlands, 2010, pp. 617–649, DOI: 10.1007/978-90-481-8831-4_15.

13 A. Cios, *et al.*, Effect of Different Wavelengths of Laser Irradiation on the Skin Cells, *Int. J. Mol. Sci.*, 2021, **22**(5), 2437, DOI: 10.3390/ijms22052437.

14 A. Limbeck, *et al.*, Methodology and applications of elemental mapping by laser induced breakdown spectroscopy, *Anal. Chim. Acta*, 2021, **1147**, 72–98, DOI: 10.1016/j.aca.2020.12.054.

15 A. Elhassan, *et al.*, Nanosecond and femtosecond Laser Induced Breakdown Spectroscopic analysis of bronze alloys, *Spectrochim. Acta, Part B*, 2008, **63**(4), 504–511, DOI: 10.1016/j.sab.2008.02.003.

16 R. Zhang, *et al.*, Laser-induced breakdown spectroscopy (LIBS) in biomedical analysis, *TrAC, Trends Anal. Chem.*, 2024, **181**, 117992, DOI: 10.1016/j.trac.2024.117992.

17 C. Sarpe, *et al.*, Identification of tumor tissue in thin pathological samples *via* femtosecond laser-induced breakdown spectroscopy and machine learning, *Sci. Rep.*, 2023, **13**(1), 9250, DOI: 10.1038/s41598-023-36155-8.

18 L. Čechová, *et al.*, Study of plasma activated water effect on heavy metal bioaccumulation by Cannabis sativa Using Laser-Induced Breakdown Spectroscopy, *Ecotoxicol. Environ. Saf.*, 2024, **283**, 116807, DOI: 10.1016/j.ecoenv.2024.116807.

19 P. Pořízka, *et al.*, Feasibility of laser-induced breakdown spectroscopy to elucidate elemental changes in human tooth ankylosis, *Spectrochim. Acta, Part B*, 2023, **206**, 106727, DOI: 10.1016/j.sab.2023.106727.

20 Z. Farka, *et al.*, Comparison of single and double pulse laser-induced breakdown spectroscopy for the detection of biomolecules tagged with photon-upconversion nanoparticles, *Anal. Chim. Acta*, 2024, **1299**, 342418, DOI: 10.1016/j.aca.2024.342418.

21 E. Zikmundová, *et al.*, Magnetic microbead-based upconversion immunoassay with laser-induced breakdown spectroscopy readout for the detection of prostate-specific antigen, *Microchim. Acta*, 2024, **191**(11), 656, DOI: 10.1007/s00604-024-06743-0.

22 S. C. Jantzi, *et al.*, Sample treatment and preparation for laser-induced breakdown spectroscopy, *Spectrochim. Acta, Part B*, 2016, **115**, 52–63, DOI: 10.1016/j.sab.2015.11.002.

23 S. Moncayo, *et al.*, Multi-elemental imaging of paraffin-embedded human samples by laser-induced breakdown spectroscopy, *Spectrochim. Acta, Part B*, 2017, **133**, 40–44, DOI: 10.1016/j.sab.2017.04.013.

24 H. Kopřivová, *et al.*, Imaging the elemental distribution within human malignant melanomas using Laser-Induced Breakdown Spectroscopy, *Anal. Chim. Acta*, 2024, **1310**, 342663, DOI: 10.1016/j.aca.2024.342663.

25 G. Galbács, Laser-Induced Breakdown Spectroscopy, *Laser-Induced Breakdown Spectroscopy in Biological, Forensic and*

Materials Sciences, Springer International Publishing, Cham, 2022, pp. 3–23, DOI: 10.1007/978-3-031-14502-5_1.
26 X. Bai, *et al.*, Experimental study of laser-induced plasma: Influence of laser fluence and pulse duration, *Spectrochim. Acta, Part B*, 2013, **87**, 27–35, DOI: 10.1016/j.sab.2013.05.019.
27 J. Buday, *et al.*, Statistical behaviour of laser-induced plasma and its complementary characteristic signals, *J. Anal. At. Spectrom.*, 2024, **39**(10), 2461–2470, DOI: 10.1039/d4ja00126e.
28 X. Li, *et al.*, Wavelength Dependence in the Analysis of Carbon Content in Coal by Nanosecond 266 nm and 1064 nm Laser Induced Breakdown Spectroscopy, *Plasma Sci. Technol.*, 2015, **17**(8), 621–624, DOI: 10.1088/1009-0630/17/8/02.
29 Q. Wang, *et al.*, Comparison of 1064 nm and 266 nm excitation of laser-induced plasmas for several types of plastics and one explosive, *Spectrochim. Acta, Part B*, 2008, **63**(10), 1011–1015, DOI: 10.1016/j.sab.2008.06.008.
30 G. Zhang, *et al.*, Optimization of experimental parameters about laser induced breakdown and measurement of soil elements, *Optik*, 2018, **165**, 87–93, DOI: 10.1016/j.ijleo.2018.03.125.
31 I. Osticioli, *et al.*, An Optimization of Parameters for Application of a Laser-Induced Breakdown Spectroscopy Microprobe for the Analysis of Works of Art, *Appl. Spectrosc.*, 2008, **62**(11), 1242–1249, DOI: 10.1366/000370208786401572.
32 T. Sato, *et al.*, Bayesian optimization of the conditions for highly sensitive detection of surface contamination by laser-induced breakdown spectroscopy, *J. Anal. At. Spectrom.*, 2023, **38**(11), 2458–2467, DOI: 10.1039/D3JA00195D.
33 H. Sun, *et al.*, Optimization and investigation of parameters for underwater gas-flow fiber-optic LIBS system, *Talanta*, 2025, **289**, 127706, DOI: 10.1016/j.talanta.2025.127706.
34 M. A. Kasem, *et al.*, Effect of the wavelength on laser induced breakdown spectrometric analysis of archaeological bone, *Spectrochim. Acta, Part B*, 2014, **101**, 26–31, DOI: 10.1016/j.sab.2014.07.010.
35 A. Fazlić, *et al.*, Investigating the effects of laser wavelengths and other ablation parameters on the detection of biogenic elements and contaminants in hydroxyapatite, *J. Anal. At. Spectrom.*, 2024, **39**(9), 2330–2339, DOI: 10.1039/D4JA00073K.
36 L. C. Nunes, *et al.*, Optimization and validation of a LIBS method for the determination of macro and micronutrients in sugar cane leaves, *J. Anal. At. Spectrom.*, 2010, **25**(9), 1453, DOI: 10.1039/c003620j.
37 V. Motto-Ros, *et al.*, Mapping nanoparticles injected into a biological tissue using laser-induced breakdown spectroscopy, *Spectrochim. Acta, Part B*, 2013, **87**, 168–174, DOI: 10.1016/j.sab.2013.05.020.
38 L. Sancey, *et al.*, Laser spectrometry for multi-elemental imaging of biological tissues, *Sci. Rep.*, 2014, **4**(1), 6065, DOI: 10.1038/srep06065.
39 A. Šindelářová, *et al.*, Methodology for the Implementation of Internal Standard to Laser-Induced Breakdown Spectroscopy Analysis of Soft Tissues, *Sensors*, 2021, **21**(3), 900, DOI: 10.3390/s21030900.
40 T. van der Lem, *et al.*, Wilhelm His Sr. and the development of paraffin embedding, *Pathologe*, 2021, **42**(S1), 55–61, DOI: 10.1007/s00292-021-00947-4.
41 A. H. Roky, *et al.*, Overview of skin cancer types and prevalence rates across continents, *Cancer Pathog. Ther.*, 2025, **3**(2), 89–100, DOI: 10.1016/j.cpt.2024.08.002.
42 J. D. Hunter, Matplotlib: A 2D Graphics Environment, *Comput. Sci. Eng.*, 2007, **9**(3), 90–95, DOI: 10.1109/MCSE.2007.55.
43 C. R. Harris, *et al.*, Array programming with NumPy, *Nature*, 2020, **585**(7825), 357–362, DOI: 10.1038/s41586-020-2649-2.
44 *The pandas development team, "pandas-dev/pandas: Pandas"*, 2025, Zenodo, DOI: 10.5281/zenodo.3509134.
45 F. Pedregosa *et al.*, Scikit-learn: Machine Learning in Python, *Journal of Machine Learning Research*, **12**, 2825–2830, 2011, https://scikit-learn.sourceforge.net.
46 S. J. Baek, *et al.*, Baseline correction using asymmetrically reweighted penalized least squares smoothing, *Analyst*, 2015, **140**(1), 250–257, DOI: 10.1039/C4AN01061B.
47 Q. Ma, *et al.*, Experimental investigation of the structure and the dynamics of nanosecond laser-induced plasma in 1-atm argon ambient gas, *Appl. Phys. Lett.*, 2013, **103**, 204101, DOI: 10.1063/1.4829628.
48 X. Bai, *et al.*, Experimental study of laser-induced plasma: Influence of laser fluence and pulse duration, *Spectrochim. Acta, Part B*, 2013, **87**, 27–35, DOI: 10.1016/j.sab.2013.05.019.
49 A. Bogaerts, *et al.*, Laser ablation of copper in different background gases: comparative study by numerical modeling and experiments, *J. Anal. At. Spectrom.*, 2006, **21**(4), 384–395, DOI: 10.1039/b514313f.
50 J. Buday, *et al.*, Determination of initial expansion energy with shadowgraphy in laser-induced breakdown spectroscopy, *Spectrochim. Acta, Part B*, 2021, **182**, 106254, DOI: 10.1016/j.sab.2021.106254.
51 F. Wolf, Chemistry and biochemistry of magnesium, *Mol. Aspects Med.*, 2003, **24**(1–3), 3–9, DOI: 10.1016/S0098-2997(02)00087-0.
52 N. Korolev, *et al.*, Competitive Binding of Mg^{2+}, Ca^{2+}, Na^{+}, and K^{+} Ions to DNA in Oriented DNA Fibers: Experimental and Monte Carlo Simulation Results, *Biophys. J.*, 1999, **77**(5), 2736–2749, DOI: 10.1016/S0006-3495(99)77107-9.
53 X. Bai, *et al.*, Morphology and characteristics of laser-induced aluminum plasma in argon and in air: A comparative study, *Spectrochim. Acta, Part B*, 2015, **113**, 158–166, DOI: 10.1016/j.sab.2015.09.023.
54 Y. Fu, *et al.*, Investigation of intrinsic origins of the signal uncertainty for laser-induced breakdown spectroscopy, *Spectrochim. Acta, Part B*, 2019, **155**, 67–78, DOI: 10.1016/j.sab.2019.03.007.

